Mg-rich amorphous to Mg-low crystalline CaCO$_3$ pathway in foraminifera

Zofia Dubicka [a,b,*,1], Maciej J. Bojanowski [c], Jelle Bijma [d], Ulf Bickmeyer [a,**,1]

[a] Ecological Chemistry, Alfred-Wegener-Institut Helmholtz-Zentrum für Polar- und Meeresforschung, Bremerhaven, 27-570, Germany
[b] University of Warsaw, Warsaw, 02-089, Poland
[c] Institute of Geological Sciences, Polish Academy of Sciences, Warsaw, Poland
[d] Marine Biogeosciences, Alfred-Wegener-Institut Helmholtz-Zentrum für Polar- und Meeresforschung, Bremerhaven, 27-570, Germany

A R T I C L E   I N F O

A B S T R A C T

Calcium carbonate minerals produced by marine organisms play a central role in the global carbon cycle and carbonate sedimentation, which influence the climate by regulating atmospheric CO$_2$ levels. Foraminifera are important marine single-celled organisms that have produced calcite shells for over 300 million years. Here, we present new observations promoting our understanding for foraminiferal biocalcification by studying *Amphistegina lessonii*. We integrated in vivo confocal autofluorescence and dye fluorescence imaging with elemental analysis of the cell supporting the concept that the calcite shells of foraminifera are produced via deposition of intracellularly formed Mg-rich amorphous calcium carbonate (Mg-ACC) particles that transform into a stable mineral phase. This process is likely accompanied by the activity of endosymbiotic microalgae and seawater-derived endocytic vesicles that provide calcification substrates such as DIC, Ca^{2+}, and Mg^{2+}. The final transformation of semi-liquid amorphous nanoparticles into a crystalline shell was associated with Mg^{2+} liberation.

1. Introduction

Biologically controlled calcification plays an important role in the evolution of Earth's surface environment, affecting the hydrosphere and atmosphere and the global carbon cycle [1]. A first-order climate control, the level of atmospheric CO$_2$, is affected by the rate of biologically-mediated marine CaCO$_3$ production. Most marine carbonate sedimentary rocks are of biogenic origin, such as modern coral reefs, Globigerina ooze covering vast areas of the modern ocean floor, Paleogene nummulite limestones, Cretaceous chalk, and Paleozoic fusulinid limestones. Therefore, understanding biocalcification processes of marine organisms is crucial for exploring carbonate sedimentation. The calcifying process of foraminifera has motivated decades of research [2–10], not only from an academic point of view of using geochemical parameters archived in biocalcite as reliable proxies for past environmental and climatic conditions, but also with respect to current challenges facing biological control over mineral growth in the context of biomimetic engineering systems [11]. Currently, there are several discordant theories concerning the fundamental aspects of foraminiferal

biomineralization mechanisms. The prevailing theory states that Rotaliida (the most numerous taxonomic group of Foraminifera) secretes calcium carbonate on an organic membrane [8,9], traditionally known as primary organic sheet (POS) [2], by attracting Ca^{2+} and bicarbonate ions that are taken up directly via *trans*-membrane transport, which fractionates against Mg [6,8]. Another theory assumes the presence of intracellular pre-calcification material in the form of a highly soluble mineral carbonate phase containing Ca and Mg [3]. Substrates for the carbonate phase (Ca^{2+}, Mg^{2+}, and CO_3^{2-}) are supposedly stored in intracellular pools, which are believed to be primarily supplied by endocytosis of seawater [4]. However, intracellular carbonate-bearing vesicles or pools have not yet been documented.

Here, we present a detailed documentation of the various physiological processes of *Amphistegina lessonii*, a rotaliid foraminifera, using complementary techniques. We integrated fluorescence imaging of living cells by confocal/multi-photon laser scanning microscopy (CLSM) with examination of fixed foraminifera at different stages of calcification by field-emission scanning electron microscopy (SEM) coupled with energy dispersive X-ray spectrometry (EDS), cryo-SEM, electron backscatter diffraction (EBSD), and a field-emission electron probe microanalyzer equipped with wavelength-dispersing spectrometers (EPM-WDS). *In vivo* experiments included labelling with various fluorescent dyes (specifically pH-sensitive LysoGlow84, membrane staining FM1-43, Mag-Fura2 AM, water-soluble and membrane-impermeable calcein, and cytosol marking Fluo-3 AM) and autofluorescence of specific structures at chosen excitation/emission wavelengths (Table 1). The results obtained allowed us to propose a new calcification model that sheds insights into the foraminifera calcification pathway and might have a substantial impact on further studies on the biocalcification process in other organisms.

2. Results

2.1. Seawater endocytosis

Three lines of evidence indicate that seawater (with relevant ions for calcification) is taken up through the shell pores of *Amphistegina lessonii* by endocytosis. First, in vivo experiments by CLSM using extracellular application of calcein, which is membrane-impermeable, showed fluorescence signals from shell pore infilling at the outside, as well as from a group of vesicles (ca. 1–2 μm in diameter) inside the cytosol (Fig. 1A and B, Movies S1 and S2). The pores were tubular shell openings across the entire shell that contained several thin (50–100 nm) nanoporous calcite layers associated with organic material (usually 5–6; Fig. 2). Pores were partly filled with reticulopodia, as shown by Fluo-3 AM staining (Fig. 2H), which stains the cytosol and SEM images (Fig. 2E–G) for high resolution. Second, the membrane probe [12] FM1-43 was used, which stains the cell membrane in contact with the environmental sea water and endocytosed vesicles. The membrane probe fluorescence emitted by the foraminiferal cell membrane and endocytotic vesicles inside the cytoplasm is demonstrated by live imaging (Fig. 1D, Movie S3). Third, SEM imaging revealed a single endocytic vesicle within the membrane of the foraminiferal pores (Fig. 2K). This suggests, together with the fact that both calcein- and FM1-43-stained moving vesicles are detected within the cytosol in large numbers just below the foraminiferal pores (Movie S4), suggesting that vacuolization and therefore endocytotic uptake of seawater occurs through the pores.

Supplementary video related to this article can be found at https://doi.org/10.1016/j.heliyon.2023.e18331

2.2. Intracellular production of Ca- and Mg-rich pools

Seawater-containing vesicles were observed in immediate proximity to relatively large (6–11 μm in size) vesicles showing autofluorescence at 405 nm excitation and 420–490 nm emission (Fig. 3A and B, Movies S5 and S6). The excitation/emission profiles of microbially induced $CaCO_3$ drops comprising ACC and vaterite published [13] and of synthetic $CaCO_3$ powder in seawater, and

Table 1
Wavelengths and dyes.

| dye	concentration during incubation	excitation nm	emission nm	source	function
BCECF AM	5 μM	Diode 405/argon 488	510–530	Thermo Fisher Scientific	pH
Lysoglow84	50 μM	Multiphoton 730	380-415/450-470	Marnas Biochemicals	pH
FM1-43	1 μM	Argon 488 or Multiphoton 1000 nm	580–620	Thermo Fisher Scientific	Membrane staining
Mag-Fura2 AM	0,5 μM	Multiphoton 730/Diode 405	416-490/495-545	Thermo Fisher Scientific	Mg^{2+} in the cytosol
Fluo-3 AM	5 μM	Argon 488	510–555	Thermo Fisher Scientific	Ca^{2+} in the cytosol
Calcein	0,7mg/10 mL	Argon 488	510–555	Thermo Fisher Scientific	Membrane impermeable water soluble dye
autofluorescence		Diode 405	420–490		$CaCO_3$, ACC
autofluorescence		DPSS 561	590–620		$CaCO_3$, ACC
autofluorescence		Diode 405/HeNe 633	650–700		Chlorophyll of symbionts
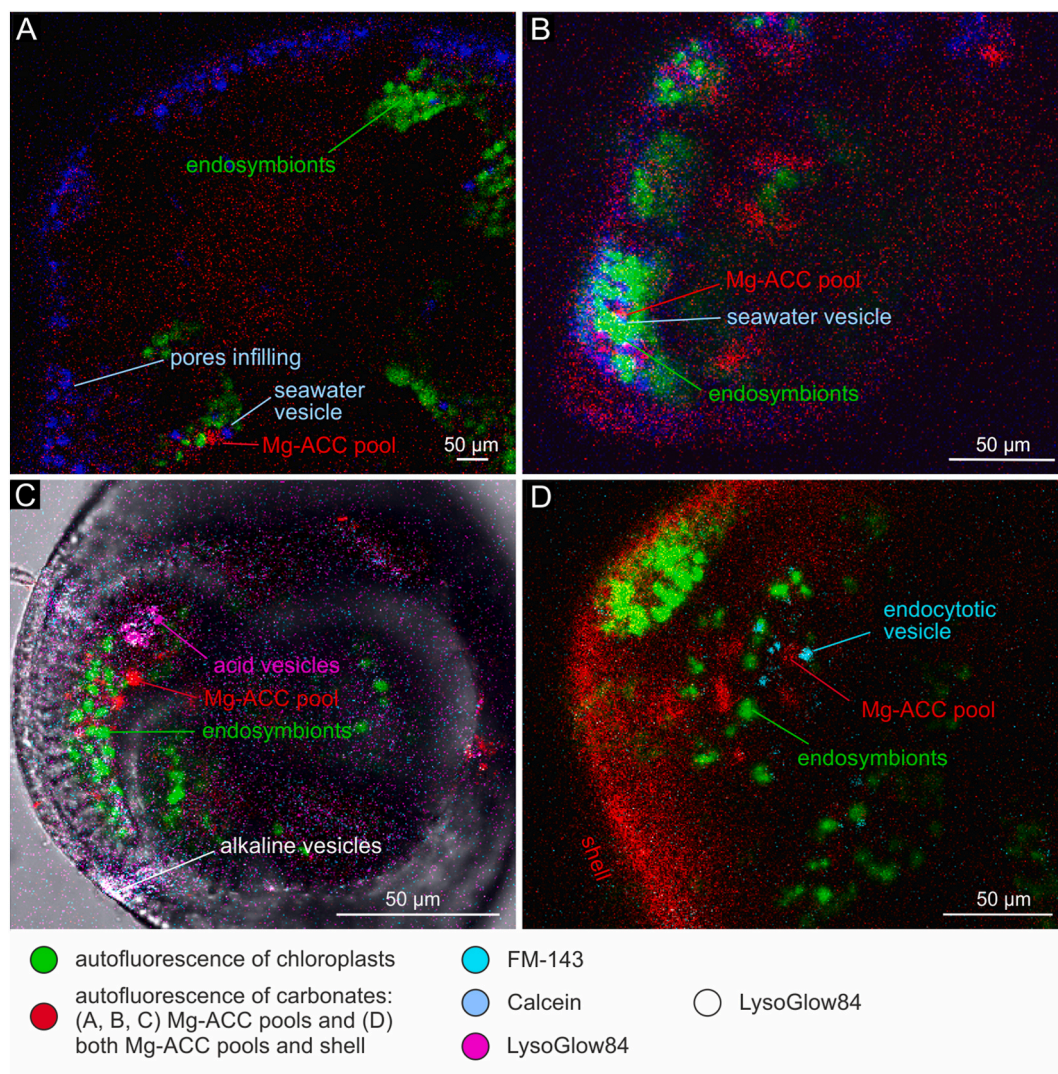
Fig. 1. Fluorescence images of living *A. lessonii* conducted by Confocal Laser Scanning Microscope. (A, B) Cell impermeable calcein (blue) indicating endocytotic seawater vesicles (note calcein-stained seawater filling the shell pores and endocytic vesicles in A), autofluorescent chloroplasts (green), and carbonate pools (likely Mg-ACC) (red); see Movie S1; (C) LysoGlow84 indicating alkaline (white) and acidic vesicles (pink), Mg-ACC pools (red), and chloroplasts (green), see Movie S7; (D) FM1-43 membrane dye indicating endocytotic vesicles (cyan), autofluorescent carbonates (red, Mg-ACC pools and shell), and chloroplasts (green), see Movie S3. (For interpretation of the references to colour in this figure legend, the reader is referred to the Web version of this article.)

synthetic colloidal Mg-rich carbonates in aqueous media composed mainly by $MgCO_3$ and $CaCO_3$ (Fig. S1) matched those of 6–11 μm sized vesicles inside *Amphistegina* cytosol implying that they were likely carbonate-containing vesicles. During SEM investigation, granules were observed in all specimens examined (>20) at different ontogenetic stages. The SEM-EDS analysis of both glutaralde-hyde- and cryo-preserved specimens revealed that the granules contained indeed Mg and Ca (Fig. 3D1, 4, and S2), whereas the EPM-WDS examination quantified the content of the main elements (Mg = 11–17 wt percent [wt. %], Ca = 5–11 wt %) and trace elements (Na, K, Sr, P, S, Mn, Fe). The latter barely exceeded the lower detection limits (Fig. 3D2, Table 2). The sum of content concentrations obtained was 65–89 wt %, with the remaining 11–35 wt % (24 wt % on average) being probably at least partly structural water. These measurements give the stoichiometry of the compound as $Ca_{(0.19-0.32)}Mg_{(0.68-0.81)}CO_3 \cdot nH_2O$, which matches that of high-Mg ACC with ~20 wt % of structural water [14]. However, because the EPM-WDS analysis is not suitable for determining the water content, the data obtained here provide a qualitative evidence. In contrast to the granules, *Amphistegina* shells are made of low-Mg calcite with Mg contents ranging between 0.3 and 0.8 wt %, being equivalent to 1.0 to 3.3 mol%, and with trace elements rarely exceeding the lower detection limits (Table 2).

Supplementary video related to this article can be found at https://doi.org/10.1016/j.heliyon.2023.e18331

The granules were strongly enriched in Mg, K, P, S, and Mn, whereas they were slightly enriched in Na and Sr, relative to the shells.
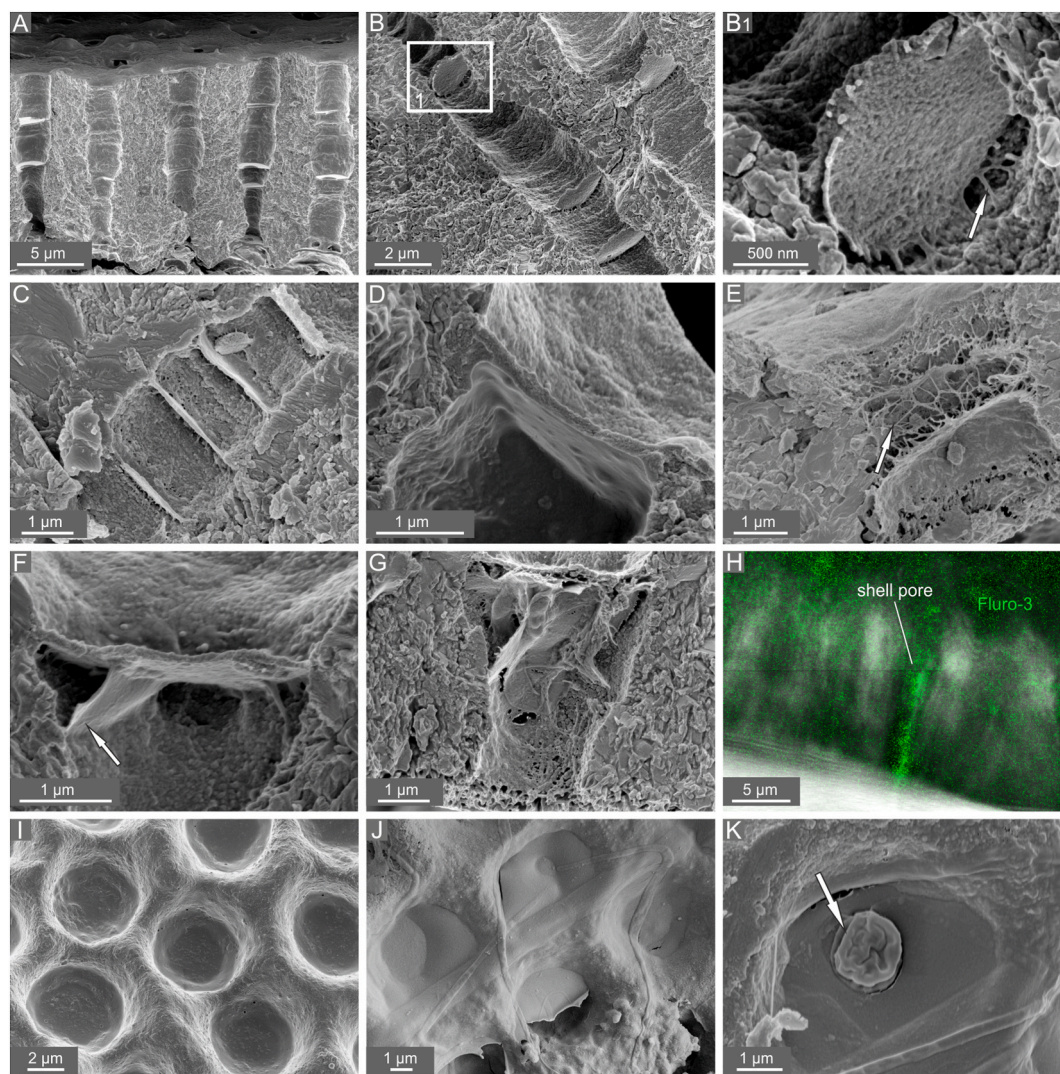
Fig. 2. SEM images of fixed *A. lessonii* (A-G, I–K) and fluorescence image of living *A. lessoni* conducted by Confocal Laser Scanning Microscope (H). Perpendicular (A, C) and oblique cross-sectional view (B) of *A. lessonii* shell showing cross sections of pores with several layers inside. Significantly magnified views of internal layers (B1, D) showing their nanogranular and porous texture, and remaining of reticulopodia (white arrows). H Fluo-3 AM (green) showing cytosol in the reticulopodia inside the pore. Front view (I–K) of the shell interior foraminiferal pores, covered with smooth organic cell membrane; note the possible endocytic vesicle marked by a white arrow (K). (For interpretation of the references to colour in this figure legend, the reader is referred to the Web version of this article.)

During electron probe microanalyzer (EPM) investigation, a 1 μm wide beam with 15 kV and 4.5 nA electron current was applied for wavelength-dispersing spectrometer (WDS)-based chemical analysis of the granules. The impact of such a focused high-energy beam was monitored by imaging the secondary electrons (SE) before and after the analyses. A well-defined pit appeared after the analysis of the spots (Fig. S3), indicating the solid nature of the material forming the granules. However, the inner wall of one granule deformed after two analyses (Figs. S3C and S3D), which may be attributed to the amorphous nature of the material. The amorphous nature of the granules was confirmed by EBSD analysis and mapping of the granules and surrounding *Amphistegina* shells (Figs. S4 and S5).

The crystalline structure characteristic of calcite was observed in the shell, whereas the results obtained in the granules were indistinguishable from those obtained in the epoxy resin, where the EBSD pattern quality was negligible and significantly lower than that of the shells. These integrated studies indicate that one population of granules are likely high-Mg amorphous calcium carbonate (Mg-ACC)-bearing pools occurring within the cytosol.

The CaMg-rich pools were in constant motion within the cytosol (Movies S5 and S6). Numerous pools were spotted at night which were hardly visible during the daytime and were accompanied by symbiont chloroplasts showing the typical autofluorescence of chlorophyll, indicating microalgae. This suggests that postulated Mg-ACC production in *Amphistegina* is related to symbiont metabolism [3] and, thus, the process is likely light/dark-dependent. The pools are also accompanied by the endocytic seawater vesicles
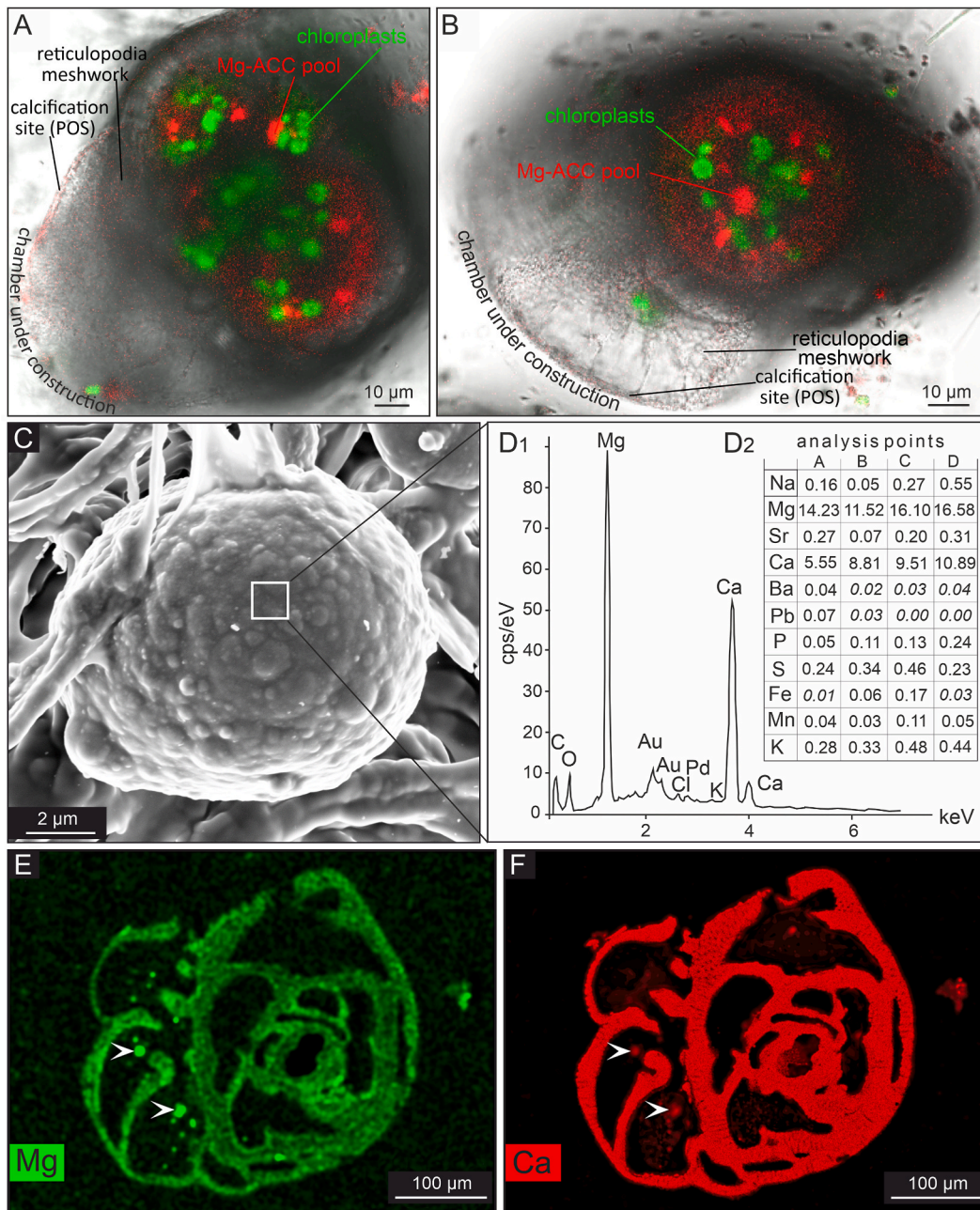
analysis points

	A	B	C	D
Na	0.16	0.05	0.27	0.55
Mg	14.23	11.52	16.10	16.58
Sr	0.27	0.07	0.20	0.31
Ca	5.55	8.81	9.51	10.89
Ba	0.04	0.02	0.03	0.04
Pb	0.07	0.03	0.00	0.00
P	0.05	0.11	0.13	0.24
S	0.24	0.34	0.46	0.23
Fe	0.01	0.06	0.17	0.03
Mn	0.04	0.03	0.11	0.05
K	0.28	0.33	0.48	0.44

Fig. 3. CaMg-rich pools of *A. lessonii.* (A, B) Autofluorescence images of selected specimens during new chamber formation showing carbonate (likely Mg-ACC) (red) and symbiotic chloroplasts (green), see Movie S6; (C) SEM image of a CaMg-rich pool; (D) Chemical composition of CaMg-rich pools: EDS spectrum (D1) and weight percent (wt. %) content of some main and trace elements measured in four granules with the use of EPM-WDS (D2). EDS mapping showing higher Mg (E) and lower Ca content (F) in the carbonate pools (marked with arrows) than in the crystalline shell. (For interpretation of the references to colour in this figure legend, the reader is referred to the Web version of this article.)

described above as well as a group of vesicles (ca. 1–2 μm in size) that are permanently moving through the cytosol in random directions and are detected by pH-sensitive fluorescent dyes [LysoGlow84 (Fig. 1E indicating both more alkaline and more acidic vesicles, Movie S7) and BCECF AM (Movie S8)]. All these components (seawater vesicles, microalgal symbionts, and acidic vesicles) are likely involved in the calcification process and their possible functions are discussed below.

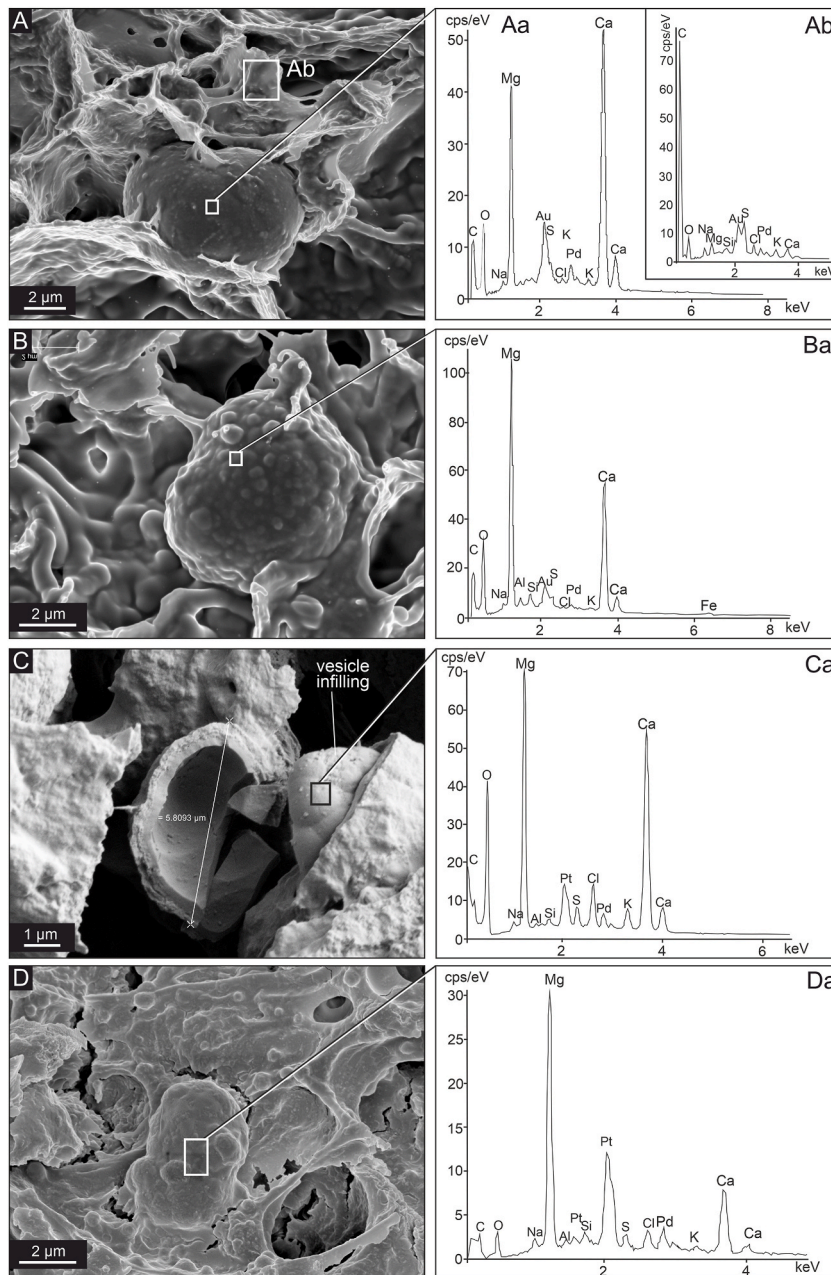Supplementary video related to this article can be found at https://doi.org/10.1016/j.heliyon.2023.e18331

Fig. 4. CaMg-rich pools of *A. lessonii*. SEM images (A–D) and energy dispersive spectroscopy (EDS) spectra (Aa-Da) indicating chemical composition of fixed CaMg-rich pools, likely Mg-rich amorphous calcium carbonate pools, inside the *A. lessonii* cytosol and of the cytoplasm that surrounds the pools (Ab). Au, Pd and Pt peaks are related to coating of samples prior to SEM analysis; cps/eV: counts per second per electron-volt.

2.3. From amorphous calcification precursor into a crystalline shell

Vesicles that showed the carbonate autofluorescence signature at 405 nm excitation and 420–490 emission were transported to the shell aperture, where they gradually disintegrated (Fig. 3B, Movie S6) and likely released their content as nanovesicles bearing (Movie S10) calcification precursor amorphous material, likely in the form of Mg-ACC. Subsequent batches of nanovesicles, as visible by their autofluorescence typical for biocarbonates (induced by 405 [13] nm or 561 nm [15]), were transported by the cytoskeleton (Fig. 5C and S6, Movie S9) to a new chamber construction site, defined by an organic sheet (Fig. S7, Movie S10), until the wall was completed. This is the place where the amorphous semi-liquid (Movie S10) nanoparticles (~20–40 nm in diameter) assemble and integrate into a crystalline shell. This final process of shell construction is likely linked to the release of Mg^{2+} as documented by Mag-Fura2 AM (Fig. 5D, Movie S11), which clearly detected Mg^{2+} close to the shell construction sites shown in time-lapse imaging.

Table 2

Elemental composition of *Amphistegina lessoni* shells and granules found within them - obtained with the use of EPM-WDS.

Amphistegina shells

Analysis point	Raw results in wt. %										
	Na	Mg	Sr	Ca	Ba	Pb	P	S	Fe	Mn	K
2/1	0.214	0.797	0.161	38.975	0.043	0.000	0.017	0.034	0.011	0.000	0.002
3/1	0.155	0.381	0.140	39.957	0.000	0.010	0.016	0.015	0.008	0.016	0.000
4/1	0.279	0.260	0.210	40.636	0.000	0.000	0.023	0.016	0.022	0.010	0.000
9/1	0.188	0.468	0.155	39.067	0.000	0.065	0.019	0.024	0.000	0.000	0.015
10/1	0.213	0.807	0.194	38.588	0.059	0.002	0.006	0.073	0.006	0.003	0.017
11/1	0.213	0.420	0.318	39.152	0.036	0.026	0.010	0.029	0.000	0.000	0.012

Granules

Analysis point	Raw results in wt. %										
	Na	Mg	Sr	Ca	Ba	Pb	P	S	Fe	Mn	K
1/1	0.16	14.23	0.27	5.55	0.04	0.07	0.05	0.24	0.01	0.04	0.28
6/1	0.05	11.52	0.07	8.81	0.02	0.03	0.11	0.34	0.06	0.03	0.33
8/1	0.27	16.10	0.20	9.51	0.03	0.00	0.13	0.46	0.17	0.11	0.48
12/1	0.55	16.58	0.31	10.89	0.04	0.00	0.24	0.23	0.03	0.05	0.44

Amphistegina shells

Analysis point	Calculated concentrations of oxides in wt. % (not normalized)												
	Na_2O	MgO	SrO	CaO	BaO	PbO	P_2O_5	SO_2	FeO	MnO	K_2O	CO_2	Total
2/1	0.29	1.32	0.19	54.53	bdl	bdl	bdl	0.07	bdl	bdl	bdl	44.57	101.0
3/1	0.21	0.63	0.17	55.91	bdl	bdl	bdl	0.03	bdl	bdl	bdl	44.81	101.8
4/1	0.38	0.43	0.25	56.86	bdl	bdl	0.05	bdl	bdl	bdl	bdl	45.48	103.4
9/1	0.25	0.78	0.18	54.66	bdl	0.07	bdl	0.05	bdl	bdl	0.02	44.06	100.1
10/1	0.29	1.34	0.23	53.99	0.07	bdl	bdl	0.15	bdl	bdl	0.02	44.26	100.3
11/1	0.29	0.70	0.38	54.78	bdl	bdl	bdl	0.06	bdl	bdl	bdl	44.16	100.4

Granules

Analysis point	Calculated concentrations of oxides in wt. % (not normalized)												
	Na_2O	MgO	SrO	CaO	BaO	PbO	P_2O_5	SO_2	FeO	MnO	K_2O	CO_2	Total
1/1	0.22	23.60	0.32	7.76	0.04	0.07	0.11	0.48	bdl	0.06	0.33	32.73	65.7
6/1	0.07	19.11	0.08	12.33	bdl	bdl	0.26	0.67	0.08	0.04	0.40	31.43	64.5
8/1	0.37	26.71	0.24	13.30	bdl	bdl	0.30	0.93	0.22	0.14	0.57	41.18	84.0
12/1	0.74	27.49	0.37	15.24	bdl	bdl	0.55	0.47	bdl	0.07	0.53	43.43	88.9

Values in italics are below the detection limit. bdl - below the detection limit.

Supplementary video related to this article can be found at https://doi.org/10.1016/j.heliyon.2023.e18331

The entire calcification process, beginning with the transfer of substrates from the surrounding seawater into vesicles inside the cell via endocytosis, through the formation and transport of CaMg-rich pools to the eventual shell construction, was demonstrated by the fluorescence of calcein. The peak of calcein at approximately 520 nm was recorded by wavelength scans in both seawater (Fig. S1E) and Mg-ACC (Fig. S1D), whereas mixed fluorescence characteristic of carbonate and calcein was observed in the newly built chambers (Fig. S1F).

3. Discussion

3.1. CaMg-rich pools to crystalline shell transition

Our integrated study, especially confocal autofluorescence (exc. 405 nm, em. 420–490 nm), elemental, and EBSD analysis of intracellular 6–11 µm sized vesicles indicate that they are likely filled by amorphous Mg-rich ACC. The fluorescent signatures of the pools detected inside *Amphistegina* cells during in vivo studies match an autofluorescence emission (420–490) of microbially induced $CaCO_3$ drops including ACC and vaterite excited by 405 nm [13]. Moreover, autofluorescence spectra under UV irradiation of biologically mediated synthetized calcium carbonate/CD hybrid composites in the form of spherical nanoparticles [16] also fit exactly to fluorescence spectra of *Amphistegina's* CaMg-rich pools. Comparable autofluorescence has also been documented for biocalcite formed through mediation by Geobacillus bacterium [17]. The size of Mg- and Ca-rich particles in the cytoplasm of *Amphistegina* corresponds to recently presented pools detected by cryo-SEM and EDS correlative method [18]. Mg-ACC in these pools is likely preserved in the form of a semi-liquid or gel-like phase. Stabilization of this paradoxically unstable phase is apparently achieved by the relatively high content of Mg, which prevents its transformation into a crystalline phase [19,20]. High-Mg ACC materials are widely accepted precursors in most biocalcification processes [21,22]. However, most of these studies were based on theoretical assumptions and on experimentally precipitated ACC instead of ACC being naturally formed by living organisms. To date, intracellular ACC pools have
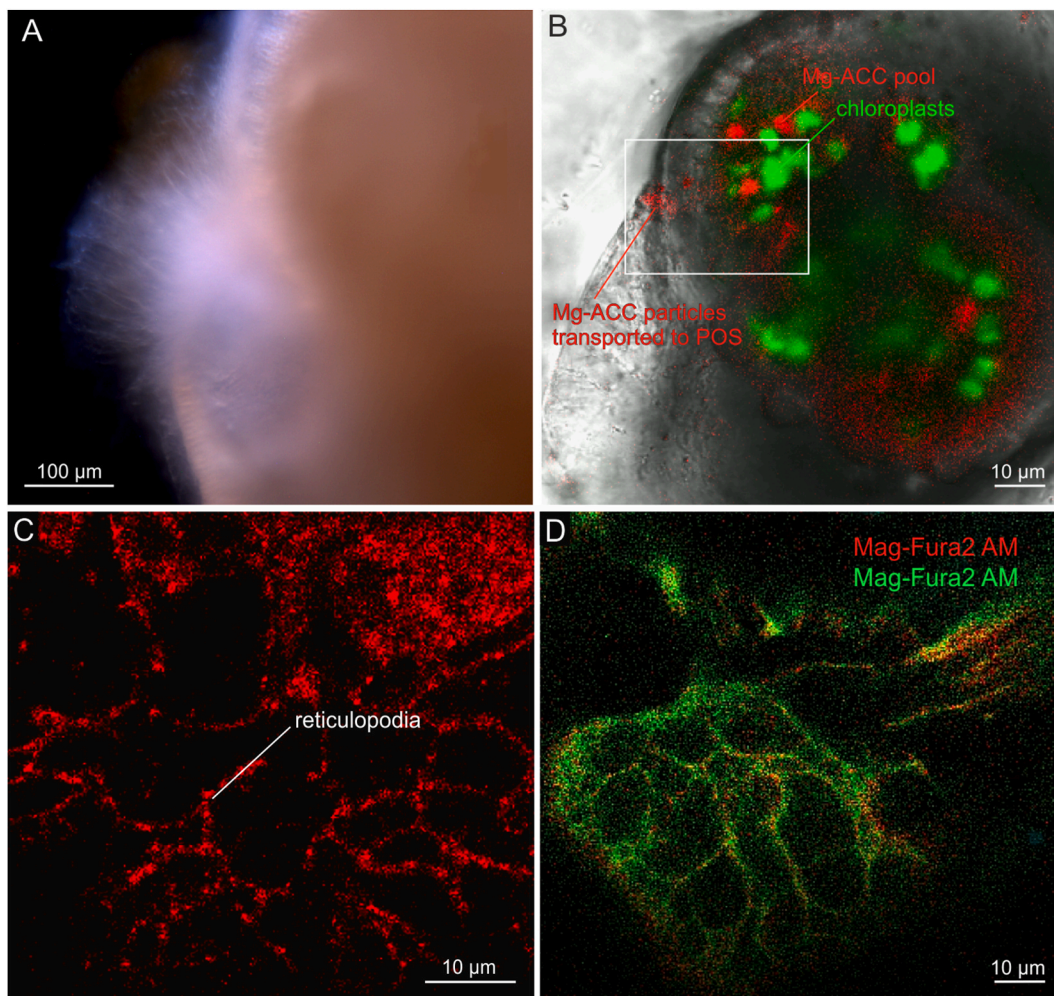
Fig. 5. *A. lessonii* **during new chamber formation**. Stereo microscope image (A) and Confocal Laser Scanning Microscope images (B–D) showing: (A) milky-white appearance of reticulopodia during shell construction, (B) autofluorescence of Mg-ACC (red) and symbiontic chloroplasts (green), (C) autofluorescence of reticulopodia transporting carbonate bearing nanovesicles (red, see also Movie S9), (D) Mag-Fura2 AM staining showing excess Mg^{2+} in red and second wavelength excitation in green (see also Movie S11). (For interpretation of the references to colour in this figure legend, the reader is referred to the Web version of this article.)

been shown only in sea urchin larvae [23] and cyanobacteria [24]. Jacob et al. [25] suggested that ACC is the most likely source material for vaterite, a metastable $CaCO_3$ polymorph found in planktic foraminifera. Once the CaMg-rich pools of *Amphistegina* are completed, they are transported close to the shell aperture, becoming a source of nanometer-sized particles, possibly released as nanovesicles, and transported to the primary organic sheets (POS) (Movies S9 and S10, Fig. S6). These nanovesicles that carry the autofluorescence characteristics of carbonates [13,14] are distributed by dynamic F-actin structures [9] to the site of new chamber formation (Movie S9). EDS elemental analysis showed significant amounts of Mg and Ca in nanogranules transported by reticulopodia, while optical microscopy imaging showed a milky-white appearance, characteristic for ACC which is a colloidal "milky" fluid [26], of reticulopodia (Fig. 5A). The final carbonate nanoparticles are deposited, aggregated, and crystallized within the organic sheet in the shape of a new chamber (Fig. 6).

Shell formation in *Amphistegina lessonii* is an example of aggregation of semi-liquid nanoparticles that transform into a crystalline biomaterial, which is now becoming accepted as the main biological strategy in most invertebrates that form shells or cuticles and vertebrates that mineralize bones and teeth [22,27,28]. While this model of crystallization has been described in various biominerals [29], the full mechanism of the transformation of amorphous particles into a crystalline material is still poorly understood. Our Mag-Fura2 AM dye experiments showed that Mg^{2+} ion liberation in the final stage of chamber formation (Movie S11) corresponds to drastic changes in the chemical composition of foraminiferal carbonate from very high-Mg (73.6 mol % on average) in the granules detected inside the cytosol to low-Mg calcite (2.1 mol % on average) in the *Amphistegina* shells (Table 2, see also [30]). The very low content of Mg in Rotaliid shells in relation to its much higher concentration in seawater has led to the commonly accepted hypothesis that *trans*-membrane transport in foraminifera at the calcification site "fractionates strongly against Mg" [6,31]. Mg ions are also likely
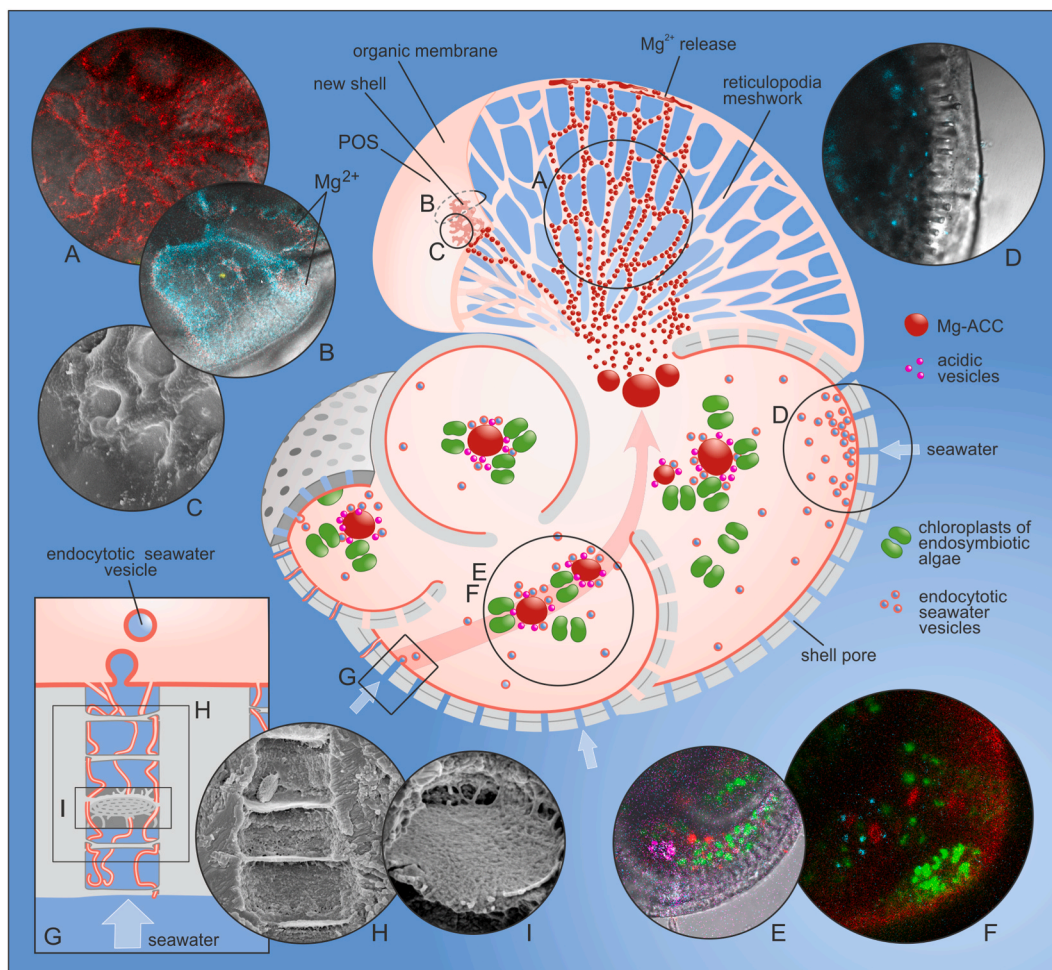
Fig. 6. Foraminiferal biomineralization (Rotaliida) model. Seawater passes through the pores that contain several internal layers (G, H, I) and enters the cytosol as vesicles (D). Proposed Mg-ACC pools accompanied by acidic vesicles and symbiotic chloroplasts are formed partly from seawater vesicles inside the cytosol (E, F). The pools disintegrate into nanogranules that are transported by reticulopodia (A) to the new chamber construction sites, where they are transformed into low-Mg calcite shell (C) and excess of Mg^{2+} is liberated (B). (A) Autofluorescence (AF) of reticulopodia transporting Mg-ACC-bearing nanovesicles. (B) Mag-Fura2 AM staining showing excess Mg^{2+} in red and second wavelength excitation in cyan. (C) SEM image of the POS with a partially formed shell. (D) Cell impermeable membrane FM1-43 staining excited in blue showing endocytotic seawater vesicles inside the cytosol. (E) LysoGlow84 staining (pink) showing acidic vesicles, autofluorescent Mg-ACC pools (red), and symbiotic chloroplasts (green) inside the cytosol. (F) FM1-43 staining indicating endocytotic vesicles (cyan), autofluorescent carbonates (both shell and Mg-ACC pools, red), and symbiotic chloroplasts (green). (G) Sketch of the pore section. (H, I) SEM images of the cross-sectional view of *Amphistegina* shell showing shell pore with several layers inside (H) and significantly magnified view of one of the internal layer (I). (For interpretation of the references to colour in this figure legend, the reader is referred to the Web version of this article.)

removed from the primary mesenchymal cells (PMCs) of sea urchin larvae during calcite spicule formation [32]. We show that Mg is taken up by foraminifera and plays an important role in the biomineralization process by enabling the maintenance and transport of an amorphous carbonate precursor. Mg^{2+} ions are eventually released during the final stage of *Amphistegina's* shell crystallization, where the nanoparticles of gel-like carbonate material are assembled, aggregated, and transformed into a crystalline structure. This interpretation is supported by the experiments of Blue et al. [33], showing the transformation of synthetized ACC into solid calcite coinciding with Mg^{2+} release. Furthermore, Rodriguez-Blanco et al. [34] documented the acceleration of the monohydrocalcite ripening reaction, which translated into a rapid growth in particle size and the formation of highly crystalline low-Mg monohydrocalcite as a consequence of Mg removal from the aqueous solution.

3.2. Sources of substrates and conditions favoring calcification

A fundamental requirement for all calcification processes is the buildup of Ca^{2+} and dissolved inorganic carbon (DIC, i.e. CO_2, HCO_3^-, CO_3^{2-}) via cellular transport mechanisms [31]. In *Amphistegina*, Ca and Mg, as well as some trace elements essential for calcification, apparently originate directly from seawater (Fig. 6), as documented by our membrane-impermeable calcein dye

experiment showing the pathway of calcein from seawater via CaMg-rich pools into the shell (Fig. S1). This is consistent with the previous report of calcein incorporation into newly built chamber [35,36]. Seawater is primarily taken up by endocytosis, as shown by calcein- and FM1-43-stained vesicles that form in large numbers just below the pores and are found adjacent to the CaMg-rich pools. Endocytotic seawater vesicles were discussed in relation to foraminiferal biocalcification process [3,4] and are also thought to be key players in the ion supply for sea urchin larvae calcification [37], although Ca^{2+} channels have also been postulated [38]. Pores in foraminifera enable seawater uptake, but the nanoporous calcite layers within them (Figs. 6I and 2A-G) might also serve as a multilayer filter against bacteria and some larger molecules. Endocytosis is the non-selective transport of seawater into foraminiferal cells, which had already been postulated by Bentov et al. [4], but was later questioned [6] in the context of the large amount of Ca^{2+} required to produce foraminiferal shells. However, the continuity and high efficiency of endocytosis, high number of pores (shown by the large number of endocytic vacuoles observed with FM1-43 staining, Movie S4), and low frequency of new chamber formation (max. one per day in juveniles and much less in adult forms), raises the question of whether an additional Ca^{2+} concentration mechanism is required.

As the DIC concentration in seawater is several times lower than that of Ca^{2+}, DIC is the limiting compound for $CaCO_3$ precipitation and requires an additional source. In *Amphistegina*, DIC for calcification is most likely produced from the metabolism of both the foraminiferal cell [38] and its endosymbiotic algae surrounding CaMg-rich vesicles (Movies S5 and S6). This hypothesis is also supported by the fact that the formation of both intracellular CaMg-rich pools and new shells takes place exclusively during night-time (see also [9]) when CO_2 is accumulated as a result of ongoing respiration and halted photosynthesis in endosymbiotic algae. Due to the long diffusion distances in large foraminifera, cells may face the problem to remove CO_2 originating from cell metabolism and from the metabolism of their symbionts. However, the O_2 supply of large cells may be accomplished by endocytotic uptake of seawater in the absence of photosynthetically produced O_2. Excess Ca^{2+} and Mg^{2+} taken up by endocytosis and excess CO_2 accumulated during the dark phase are removed by the production of $(Mg–Ca)CO_3$ (Mg-ACC) and by shell being built in the dark. This could be considered as the removal of cellular garbage [39].

This additional carbon source from cell respiration meets the demand for DIC, given its limited availability in seawater. For comparison, in sea urchin embryos, which do not possess endosymbionts, 60% of DIC used for ACC production is absorbed from metabolic CO_2, whereas only 40% is derived from seawater [38]. Extracellular membrane-bound carbonic anhydrases (Cara 7), coupled to HCO_3^- uptake mechanism, perform an important role during calcification process in sea urchin larvae as it mitigates the loss of carbon and decreases the cellular proton load [40].

Carbonic anhydrases (CA), both cytosolic and extracellular, play a central role in the cellular carbon concentration from metabolic CO_2 and thus in calcification of marine organisms [40,41] by catalyzing the reversible hydration of CO_2 to form H_2CO_3 that then dissociates into HCO_3^- and CO_3^{2-}. The direction of the process is pH dependent. The role of CA in foraminiferal calcification would be an interesting perspective for future studies.

Apart from substrates, the biocalcification process requires also pH regulation by removing protons from the mineralization front [42]. In *Amphistegina*, pH regulation is apparently linked to the presence of acidic vesicles in immediate proximity to the Mg-ACC pools detected by fluorescence imaging using LysoGlow84 [43] and BCECF AM probes (Movies S7 and S8). This process might be partially controlled by the V-type H^+-ATPase enzyme, as documented by Toyofoku et al. [7] in foraminifera and Hu et al. [44] in sea urchin larvae that also produce intracellular carbonates. H^+-ATPase might concentrate H^+ in the detected foraminiferal low pH vesicles followed by exocytosis to seawater. In sea urchin embryos, pH homeostasis in calcifying primary mesenchyme cells (PMCs) is driven by the Na^+/H^+ exchange (NHE) mechanism [44,45,46] in a resting state. However, during active calcification process, otopetrin proton channels (otop2l) are used to remove protons from the cytosol [47]. Coccolithophores were also demonstrated to employ proton H_v1 channels to remove protons that have been generated by the calcification process [48]. In foraminifera, pH regulation has been interpreted in terms of extracellular matrix mineralization theory [7,49] and pH changes were sought at the vicinity of the primary organic sheets (POS), where the new chamber is formed. However, the decrease in pH observed in the surrounding seawater outside the shell instead of a local pH decrease in the newly constructed chamber [7] suggests that protons are released from the foraminiferal endoplasm and would rather support the intracellular carbonate production. As the cellular pH of most eukaryotic cells is approximately 7.3, and seawater may have a pH of 8.2, the driving force for H^+ removal from the cell by H^+ channels may proceed by a relatively low cellular membrane potential (work in progress) calculated by the Nernst potential for H^+.

There are two main gaps in this study that should be addressed in future research. First, the CaMg-rich pool infilling could be studied in detail by additional techniques to better understand its physical and chemical properties. Second, is the lack of exact pH calculation at the *Amphistegina* mineralization front.

4. Conclusions

The biomineralization process of *Amphistegina* is fueled by Mg- and Ca-rich amorphous calcite precursor that is produced within intracellular pools. This amorphous material is likely in the form of Mg-ACC, however to understand its real nature future research needs to apply additional techniques. The source of relevant ions (Ca^{2+}, Mg^{2+}, and CO_3^{2-}) for the process are apparently the endocytic seawater vesicles and endosymbiotic algae. The final shell production is associated with Mg^{2+} liberation and the activity of the cytoskeleton that shape/stabilize the POS and carry semi-liquid carbonate nanoparticles.

The biomineralization model presented here do not include the process of production of CaMg-rich pools. Therefore, a variety of research goals are of interest, such as the ion-exchange mechanism across the pool membrane, the pH of the pools and the potential role of carbonic anhydrases in carbonate production.

Author contribution statement

Zofia Dubicka, Ulf Bickmeyer: Conceived and designed the experiments; Performed the experiments; Analyzed and interpreted the data; Wrote the paper.

Maciej J. Bojanowski: Performed the experiments; Analyzed and interpreted the data; Wrote the paper.

Jelle Bijma: Analyzed and interpreted the data; Wrote the paper.

Funding statement

Data availability statement

Data included in article/supp. material/referenced in article.

Declaration of competing interest

The authors declare that they have no known competing financial interests or personal relationships that could have appeared to influence the work reported in this paper.

Acknowledgments

Appendix ASupplementary data

Supplementary data to this article can be found online at https://doi.org/10.1016/j.heliyon.2023.e18331.

Appendix

STAR methods
    Resource availability
        Lead contact

Further information and requests for resources should be directed to and will be fulfilled by the lead contact, Zofia Dubicka (z.dubicka@uw.edu.pl).

Materials availability

This study did not generate new unique materials.

Data and code availability

Any additional information required to reanalyze the data reported in this paper is available from the lead contact upon request.

Method details
    Foraminifera culture

Living foraminifera, collected from the coral reef aquarium in the Burgers Zoo (The Netherlands), were kept in a 10 L aquarium containing natural North Sea water (NSW) at a temperature of 24 °C and a 12:12 h light:dark cycle. Both juveniles and adults of *A. lessonii* were transferred with a fine brush or plastic pipette into 4 mL optical quality glass bottom dishes with room temperature NSW (Tyszka et al., 2019) to allow regular observation with a binocular and bright field microscope (Zeiss Axiovert 200 M), as well as confocal microscopy experiments.

In vivo fluorescence imaging

Live fluorescence imaging of *A. lessonii* was performed using a Leica SP5 confocal laser scanning microscope (CLSM) equipped with an argon laser, helium-neon-, neon-, diode-, and multiphoton Mai Tai laser (Spectra Physics). Fluorescence experiments exploited both the natural autofluorescence of cell structures ($CaCO_3$, chlorophyll fluorescence of symbionts) as well as labelling techniques (Table 1) using pH-sensitive dyes BCECF AM (5 μM, exc. 405/488 nm, em. 510–530 nm, Invitrogen, incubation time: 2h) and LysoGlow84 (50 μM exc. 340 nm/em. 380–415 nm and 450–470 nm, Marnas Biochemicals Bremerhaven, incubation time: 2h), FM1-43 membrane stain (1 μM, exc. 488 nm, em. 580–620 nm, Invitrogen, incubation time: 24h), Mg^{2+}-sensitive Mag-Fura2 AM (0.5 μM exc. MP730 nm, em. 416–490 nm, exc. 405 nm 495–545 nm, Invitrogen, incubation time: 0.5 h), seawater staining with membrane impermeable calcein (0.7 mg/10 mL, exc. 488 nm, em. 510–555 nm, incubation time: 24 h, just before the experiment, the seawater containing calcein was removed with a pipette), and cell-permeant dye Fluo-3 AM (5 μM, exc. 488 nm, em. 510–555 nm; Invitrogen, incubation time: 2 h). All experiments were replicated with at least several individuals. For comparative purposes, colloidal carbonate solutions in the aquatic medium have been prepared that contains similar element proportions as detected in living *Amphistegina* $CaCO_3$ 1,387g, $MgCO_3$ 4.982g, $MnSO_4$ X H_2O 12,3 mg, KH_2PO_4 97,6 mg, $NaSO_4$ 88,75 mg in 35 mL H_2O, pH~9.

Scanning electron microscopy (SEM) with energy dispersive spectroscopy (EDS)

Foraminifera were fixed at different stages of the calcification process by treatment with 3% glutaraldehyde for 5–7 s and then dehydrated by a few seconds of treatment with an ethanol/distilled water mixture whose alcohol concentration increased in each step (30%, 50%, 70%, and 99%). Fixed foraminifera were examined using a Zeiss Σigma VP field-emission scanning electron microscope (SEM) coupled with an energy dispersive X-ray spectrometer (EDS). The selected specimens were gently broken with a needle to examine the interior of the shell/cell. All the specimens were coated with a 5–10 nm thick platinum/palladium (80%/20%) layer before examination.

Electron probe microanalysis (EPM) with wavelength-dispersing spectrometery (WDS)

Quantitative standards-based chemical analysis of granules and shells was carried out on polished sections fixed and soaked in epoxy resin *Amphistegina* cells using Cameca SXFiveFE (produced at Gennevilliers Cedex, France) field-emission electron probe microanalyzer (EPM) equipped with five wavelength-dispersing spectrometers (WDS). The sections were coated with a 20 nm carbon layer prior to analysis. The acceleration voltage was 15 kV and beam current was reduced with a condenser lens-projected beam on splash aperture to 4.5 nA. An objective aperture of 200 μm without a beam regulator was used because the Schottky field-emission electron emitter was correctly monitored and adjusted to prevent overheating. The stability of the unregulated beam has no drift or fluctuation, which changes the beam current in a long (an hour) or short time (a few seconds) by more than 0.4% from the initial value. The final electron beam on the sample was defocused to 1–5 μm in diameter depending on the available object size. The following diffracting crystals and X-ray lines (in brackets) were used: TAP (Na Kα, Mg Kα, Si Kα, Sr Lα, and Al Kα), LPET (Ca Kα, Ba Lα, Pb Mα, P Kα, S Kα, and K Kα), and LLIF (Fe Kα and Mn Kα). The following standard substances were used: Albite for Na, MgO for Mg, $SrSO_4$ for S and Sr, Diopside for Si and Ca, $BaSO_4$ for Ba, PbTe for Pb, Apatite (Durango) for P, Fe_2O_3 for Fe, Rhodonite for Mn, Al_2O_3 for Al, Orthoclase for K. Recalculation of X-ray net counts into weight percent (wt. %) was done using Cameca Peaksight 6.5 software using the following settings: matrix correction with a built-in X–PHI model of Merlet (1994), Cameca superset of mass absorption coefficients (MAC), analysis mode set to "Matrix Definition and Stochiometry", where for a better matrix correction of the analyzed elements, a static 12 wt % of theoretical C was added. After matrix correction, the C results were recalculated stoichiometrically to be charge-balanced with other elements.

SEM with electron back-scattered diffraction (EBDS) mapping

Prior to the EBSD analysis, sections previously used for the EPM investigation were re-polished to remove the carbon coating using a vibratory polisher with a 0.25 μm colloidal diamond suspension. Then, the sections were coated with a 4 nm carbon layer and framed with a highly conductive copper tape to reduce charging effects. The analysis was conducted using a Zeiss Auriga 60 field-emission SEM equipped with a e^- Flash Bruker EBSD detector. The samples were tilted by 70°, and image tilt correction was applied using ZEISS SmartSEM software. The analysis was carried out in a high vacuum using an acceleration voltage of 15 kV. A 400 × 300 EBSD pattern resolution was acquired in rectangular areas ranging between 800 and 2100 μm^2. The acquisition time of the EBSD maps was varied from 10 to 18 min. For phase identification of calcite, the following crystallographic parameters were used: R3c, a = 4.99 Å, c = 17.061 Å.

Cryo-SEM with EDS

The analysis was carried out using a ZEISS Auriga 60 field emission scanning electron microscope (FE-SEM). The samples were frozen to −190 °C using a Quorum PP3010 Cryo-SEM system. The samples were analyzed using a Bruker XFlash 6|30 EDS spectrometer at an acceleration voltage of 15 kV, 2s counting time (live time). The measurement time was set to only 2s to avoid damaging or destruction of fragile frozen samples, hence the high noise-to-signal ratio. The samples were examined without a conductive coating. Cryo-fixation, where foraminifera were rapidly frozen, provide cell preservation in a vitreous state. All SEM-based and EPM investigations were performed in the Laboratory of Electron Microscopy, Microanalysis, and X-ray diffraction at the Faculty of Geology, University of Warsaw, Poland.

References

[1] J.W. Morse, F.T. Mackenzie, Sedimentary carbonates in the evolution of earth's surface environment, in: Geochemistry of Sedimentary Carbonates, Development in Sedymentology, vol. 48, Elsevier Science Verlag), 1990, pp. 511–598.

[2] Ch Hemleben, O.R. Anderson, W.U. Berthold, M. Spindler, Calcification and chamber formation in Foraminifera-A brief overview, in: B.C. Leadbeater, R. Riding R (Eds.), Biomineralization in Lower Plants and Animals: the Systematics Association 3D, Special, 1986, pp. 237–249.

[3] J. Erez, The source of ions for biomineralization in foraminifera and their implications for paleoceanographic proxies, Rev. Mineral. Geochem. 54 (2003) 15–149, https://doi.org/10.2113/0540115.

[4] S. Bentov, C. Brownlee, J. Erez, The role of seawater endocytosis in the biomineralization process in calcareous foraminifera, Proc. Natl. Acad. Sci. U.S.A. 106 (2009) 21500–21504, https://doi.org/10.1073/pnas.0906636106.

[5] S. Weiner, L. Addadi, Crystallization pathways in biomineralization, Annu. Rev. Mater. Res. 41 (2011) 21–40, https://doi.org/10.1146/annurev-matsci-062910-095803.

[6] G. Nehrke, N. Keul, G. Langer, L.J. de Nooijer, J. Bijma, A new model for biomineralization and trace-element signatures of Foraminifera tests, Biogeosciences 10 (2017) 6759–6767, https://doi.org/10.5194/bg-10-6759-2013.

[7] T. Toyofuku, M.Y. Matsuo, L.J. de Nooijer, Y. Nagai, S. Kawada, K. Fujita, G.-J. Reichart, H. Nomaki, M. Tsuchiya, H. Sakaguchi, H. Kitizato, Proton pumping accompanies calcification in foraminifera, Nat. Commun. 8 (2017), 14145, https://doi.org/10.1038/ncomms14145.

[8] Y. Nagai, K. Uematsu, Ch Chen, R. Wani, J. Tyszka, T. Toyofuku, Weaving of biomineralization framework in rotaliid foraminifera: implications for paleoceanographic proxies, Biogeosciences 15 (2018) 6773, https://doi.org/10.5194/bg-15-6773-2018.

[9] J. Tyszka, U. Bickmeyer, M. Raitzsch, J. Bijma, K. Kaczmarek, A. Mewes, P. Topa, M. Janse, Form and function of F-actin during biomineralization revealed from live experiments on foraminifera, Proc. Natl. Acad. Sci. USA 116 (2019) 4111–4116, https://doi.org/10.1073/pnas.1810394116.

[10] S. de Goeyse, A.E. Webb, G.-J. Reichart, L.J. de Nooijer, Carbonic anhydrase is involved in calcification by the benthic foraminifer *Amphistegina lessonii*, Biogeosciences 18 (2021) 393–401.

[11] D.W. Green, J.-M. Lee, H.-S. Jung, Marine structural biomaterials in medical biomimicry, Tissue Eng. B Rev. 21 (2015) 438–450, https://doi.org/10.1089/ten.TEB.2015.0055.

[12] A.J. Cochilla, J.K. Angleson, W.J. Betz, Monitoring secretory membrane with fm1-43 fluorescence, Annu. Rev. Neurosci. 22 (1999) 1–10, https://doi.org/10.1146/annurev.neuro.22.1.1.

[13] N.M. Zambare, N.Y. Naser, N. Gerlach, C.B. Chang, Mineralogy of microbially induced calcium carbonate precipitates formed using single cell drop-based microfluidics, Sci. Rep. 10 (2020), 17535, 10.1038/s41598-020-73870-y.

[14] A. Koishi, A. Fernandez-Martinez, B. Ruta, M. Jimenez-Ruiz, R. Poloni, D. di Tommaso, F. Zontone, G.A. Waychunas, G. Montes-Hernandez, Role of impurities in the kinetic persistence of amorphous calcium carbonate: a nanoscopic dynamics view, J. Phys. Chem. C 122 (29) (2018) 16983–16991, 10.1021/acs.jpcc.8b05189.

[15] A.A. Abalymov, R.A. Verkhovskii, M.V. Novoselova, B.V. Parakhonskiy, D.A. Gorin, A.M. Yashchenok, G.B. Sukhorukov, Live-cell imaging by confocal Raman and fluorescence microscopy recognizes the crystal structure of calcium carbonate particles in HeLa cells, Biotechnol. J. 13 (11) (2018), e1800071, https://doi.org/10.1002/biot.201800071.

[16] S. Guo, M. Yang, M. Chen, J. Zhang, K. Liu, L. Yea, W. Gu, Bioinspired synthesis of fluorescent calcium carbonate/carbon dot hybrid composites, Dalton Trans. 44 (2015) 8232, https://doi.org/10.1039/c5dt00837a, 2015.

[17] G.M. Khalifa, K. Kahil, J. Erez, I.K. Ashiri, E. Shimoni, I. Pinkas, L. Addadi, S. Weiner, Characterization of unusual MgCa particles involved in the formation of foraminifera shells using a novel quantitative cryo SEM/EDS protocol, Acta Biomater. 77 (2018) 342–351, 10.1016/j.actbio.2018.07.026.

[18] N. Yoshida, E. Higashimura, Y. Saeki, Catalytic biomineraliᵃtion of fluorescent calcite by the thermophilic bacterium Geobacillus thermoglucosidasius, Appl. Environ. Microbiol. 76 (21) (2010) 7322–7327, 10.1128/AEM.01767-10.

[19] Y. Politi, D.R. Batchelor, P. Zaslansky, B.F. Chmelka, J.C. Weaver, I. Sagi, S. Weiner, L. Addadi, Role of magnesium ion in the stabilization of biogenic amorphous calcium carbonate: a structure-function investigation, Chem. Mater. 22 (2010) 161–166, https://doi.org/10.1021/cm902674h.

[20] E. Seknazi, S. Kozachkevich, I. Polishchuk, N.B. Stein, J. Villanova, J.-P. Suuronen, C. Dejoie, P. Zaslansky, A. Katsman, B. Pokroy, From spinodal decomposition to alternating layered structure within single crystals of biogenic magnesium calcite, Nat. Commun. 10 (2019) 4559, https://doi.org/10.1038/s41467-019-12168-8.

[21] F.C. Meldrum, H. Cölfen, Controlling mineral morphologies and structures in biological and synthetic systems, Chem. Rev. 108 (2008) 4332–4432, https://doi.org/10.1021/cr8002856.

[22] J.J. De Yoreo, P.U. Gilbert, N.A. Sommerdijk, R.L. Penn, S. Whitelam, D. Joester, H. Zhang, J.D. Rimer, A. Navrotsky, J.F. Banfield, A.F. Wallace, F.M. Michel, F.C. Meldrum, H. Cölfen, P.M. Dove, Crystallization by particle attachment in synthetic, biogenic, and geologic environments, Science 349 (2015) 6247, https://doi.org/10.1126/science.aaa6760.

[23] E. Beniash, J. Aizenberg, L. Addadi, S. Weiner, Amorphous calcium carbonate transforms into calcite during sea urchin larval spicule growth, Proc. Roy. Soc. Lond. B 264 (1997) 461–465, https://doi.org/10.1098/rspb.1997.0066.

[24] M. Blondeau, M. Sachse, C. Boulogne, C. Gillet, J.M. Guigner, F. Skouri-Panet, M. Poinsot, C. Ferard, J. Miot, K. Benzerara, Amorphous calcium carbonate granules form within an intracellular compartment in calcifying cyanobacteria, Front. Microbiol. 9 (2018) 1768, https://doi.org/10.3389/fmicb.2018.01768.

[25] D.E. Jacob, R. Wirth, O.B.A. Agbaje, O. Branson, S.M. Eggins, Planktic foraminifera form their shells via metastable carbonate phase, Nat. Commun. 8 (2017) 1265, https://doi.org/10.1038/s41467-017-00955-0.

[26] L. Gago-Duport, M.J. Briones, J.B. Rodríguez, B. Covelo, Amorphous calcium carbonate biomineralization in the earthworm's calciferous gland: pathways to the formation of crystalline phases, J. Struct. Biol. 162 (2008) 422–435, https://doi.org/10.1016/j.jsb.2008.02.007.

[27] V. Schoeppler, D. Stier, R.J. Best, C. Song, J. Turner, B.H. Savitzky, C. Ophus, M.A. Marcus, S. Zhao, K. Bustillo, I. Zlotnikov, Crystallization by amorphous particle attachment: on the evolution of texture, Adv. Mater. 33 (2021), 2101358, https://doi.org/10.1002/adma.202101358.

[28] K. Kahil, S. Weiner, L. Addadi, A. Gal, Ion pathways in biomineralization: perspectives on uptake, transport and deposition of calcium, carbonate and phosphate, J. Am. Chem. Soc. 22 (50) (2021) 21100–21112, https://doi.org/10.1021/jacs.1c09174, 143.

[29] H. Cölfen, M. Antonietti, Mesocrystals: inorganic superstructures made by highly parallel crystallization and controlled alignment, Angew. Chem. Int. Ed. 44 (2005) 5576–5591, https://doi.org/10.1002/anie.200500496.

[30] S.K. Toler, P. Hallock, S. Johan, Mg/Ca ratios in stressed foraminifera, *Amphistegina gibbosa*, from the Florida keys, Mar. Micropaleontol. 43 (2001) 199–206, https://doi.org/10.1016/S0377-8398(01)00034-2.

[31] E. Geerken, L. de Nooijer, T. Toyofuku, A. Roepert, J.J. Middelburg, M.V.M. Kienhuis, Y. Nagai, L. Polerecky, G.-J. Reichart, High precipitation rates characterize biomineralization in the benthic foraminifer *Ammonia beccarii*, Geochem. Cosmochim. Acta 318 (2022) 70–82, https://doi.org/10.1016/j.gca.2021.11.026.

[32] K. Kahil, I. Kaplan-Ashiri, S.G. Wolf, S. Rechav, S. Weiner, L. Addadi, Elemental compositions of sea urchin larval cell vesicles evaluated by cryo-STEM-EDS and cryo-SEM-EDS, Acta Biomater. 55 (2023) 482–490, https://doi.org/10.1016/j.actbio.2022.11.012.

[33] C.R. Blue, A. Giuffre, S. Mergelsberg, N. Han, J.J. De Yoreo, P.M. Dove, Chemical and physical controls on the transformation of amorphous calcium carbonate into crystalline CaCO3 polymorphs, Geochem. Cosmochim. Acta 196 (2017) 179–196, https://doi.org/10.1016/j.gca.2016.09.004.

[34] J.D. Rodriguez-Blanco, S. Shaw, P. Bots, T. Roncal-Herrero, L.G. Benning, The role of Mg in the crystallization of monohydrocalcit, Geochem. Cosmochim. Acta 127 (2014) 204–220, https://doi.org/10.1016/j.gca.2013.11.034.

[35] J.M. Bernhard, J.K. Blanks, C.J. Hintz, G.T. Chandler, Use of the fluorescent calcite marker calcein to label foraminiferal tests, J. Foraminifer. Res. 34 (2004) 96–101, https://doi.org/10.2113/0340096.

[36] J. Erez, Y. Levenson, A. Almogi-Labin, The use of the fluorescent probe Calcein to study biomineralization processes in foraminifera, Geophys. Res. Abstr. 12 (2010) EGU2010–9318.

[37] N. Vidavsky, S. Addadi, A. Schertel, D. Ben-Ezra, M. Shpigel, L. Addadi, S. Weiner, Calcium transport into the cells of the sea urchin larva in relation to spicule formation, Proc. Natl. Acad. Sci. U.S.A. 113 (2016) 12 637, https://doi.org/10.1073/pnas.1612017113, 12 642.

[38] C.S. Sikes, K. Okazaki K, R.D. Fink, Respiratory CO2 and the supply of inorganic carbon for calcification of sea urchin embryos, Comp. Biochem. Physiol. A Physiol. 70 (1981) 285–291, https://doi.org/10.1016/0300-9629(81)90181-X.

[39] E. Cordat, J.R. Casey, Bicarbonate transport in cell physiology and disease, Biochem. J. 417 (2009) 423–439, https://doi.org/10.1042/BJ20081634.

[40] A.-S. Ann-Sophie Matt, W.W. Chang, M.Y. Hu, Extracellular carbonic anhydrase activity promotes a carbon concentration mechanism in metazoan calcifying cells, Proc. Natl. Acad. Sci. USA 119 (40) (2022), e2203904119, https://doi.org/10.1073/pnas.2203904119.

[41] M.A. Rahman, T. Oomori, The role of carbonic anhydrase enzyme in the biocalcification process of coral and its resilience to global climate change, Ocean. IEEE Sydney 2010 (2010) 1–5.

[42] M.Y. Hu, J.J. Yan, I. Petersen, N. Himmerkus, M. Bleich, M. Stumpp, A Slc4 family bicarbonate transporter is critical for intracellular pH regulation and biomineralization in sea urchin embryos, Elife 7 (2018), e36600, https://doi.org/10.7554/eLife.36600.

[43] T. Mordhorst, S. Awal, S. Jordan, C. Petters, L. Sartoris, R. Dringen, U. Bickmeyer, Chemically synthesized ageladine A-derivative LysoGlow84 stains lysosomes in viable mammalian brain cells and specific structures in the marine flatworm macrostomum lignano, Mar. Drugs 13 (2015) 920–935, https://doi.org/10.3390/md13020920.

[44] M.Y. Hu, I. Petersen, W.W. Chang, C. Blurton, M. Stumpp, Cellular bicarbonate accumulation and vesicular proton transport promote calcification in the sea urchin larva, Proc. R. Soc. A B 287 (2020), 20201506, https://doi.org/10.1098/rspb.2020.1506.

[45] N. Vidavsky, S. Addadi, J. Mahamid, E. Shimoni, D. Ben-Ezra, M. Shpigel, S. Weiner, L. Addadi, Initial stages of calcium uptake and mineral deposition in sea urchin embryos, Proc. Natl. Acad. Sci. U.S.A. 111 (2014) 39–44, https://doi.org/10.1073/pnas.1312833110, 2014.

[46] M. Stumpp, M.Y. Hu, F. Melzner, M.A. Gutowska, N. Dorey, N. Himmerkus, W.C. Holtmann, S.T. Dupont, M.C. Thorndyke, M. Bleich, Acidified seawater impacts sea urchin larvae pH regulatory systems relevant for calcification, Proc. Natl. Acad. Sci. U.S.A. 109 (2012) 18, https://doi.org/10.1073/pnas.1209174109, 192–18 197.

[47] W.W. Chang, A.S. Matt, M. Schewe, M. Musinszki, S. Grüssel, J. Brandenburg, D. Garfield, M. Bleich, T. Baukrowitz, M.Y. Hu, An otopetrin family proton channel promotes cellular acid efflux critical for biomineralization in a marine calcifier, Proc. Natl. Acad. Sci. U. S. A. 118 (30) (2021), e2101378118, https://doi.org/10.1073/pnas.2101378118.

[48] A.R. Taylor, A. Chrachri, G. Wheeler, H. Goddard, C. Brownlee, A voltage-gated H$^+$ channel underlying pH homeostasis in calcifying coccolithophores, PLoS Biol. 9 (2011), e1001085, https://doi.org/10.1371/journal.pbio.1001085, 2011.

[49] L.J. de Nooijer, T. Toyofuku, H. Kitazato, Foraminifera promote calcification by elevating their intracellular pH, Proc. Natl. Acad. Sci. U.S.A. 106 (2009) 15374–15378.